The Hodgkin-Huxley Neuristor

The Hodgkin-Huxley Neuristor

A. Ascoli, E. Gemo, F. Corinto, M. Bonnin, M. Gilli, and P.P. Civalleri, *Department of Electronics and Telecommunications*, *Politecnico di Torino*, Torino, Italia

A.S. Demirkol, I. Messaris, V. Ntinas, D. Prousalis, and R. Tetzlaff, *Institut für Grundlagen der Elektrotechnik und Elektronik*, *TU Dresden*, Dresden, Germany

S. Slesazeck[a], and T. Mikolajick[a,b], [a] NaMLab gGmbH, [b] *Institut für Halbleiter- und Mikrosystemtechnik*, *TU Dresden*, Dresden, Germany

L. Chua, *Department of Electrical Engineering and Computer Sciences*, *University of California, Berkeley*, Berkeley, California, USA

***Abstract*—The electrical engineering community, interested to develop bio-inspired circuits, approaching the efficiency of the neural networks, is searching passionately for accurate yet simple electronic neurons, or neuristors for short. In recent years, the advent of volatile memristor devices, typically referred to as threshold switches, which admit a negative differential resistance under suitable polarization, similarly as the sodium and potassium ion channels across neuronal axon membranes, has opened up new exciting opportunities in neuromorphic circuit design, enabling innovative analogue electronic cells, capable to reproduce closely the intricate dynamical behaviors of biological neurons without requiring a disproportionate use of resources. The study, presented in this manuscript, achieves an important milestone in this area of research, demonstrating, through a circuit design approach based upon concepts and techniques from Dynamical System Theory, how to leverage the rich dynamics of a threshold switch, capable to boost a periodic sine-wave current signal of infinitesimal amplitude, while acting as a source of local energy, when poised on a suitable bias point, lying along the negative differential resistance branch of the respective S-shaped DC current-voltage characteristic, to induce, one after the other, the three fundamental bifurcations, governing the evolution of an electrical voltage spike from birth to extinction via the All-to-None effect across a biological axon membrane under a reverse sweep in the net synaptic current, according to the fourth-order Hodgkin-Huxley neuron model, in a second-order three-element circuit of unprecedented simplicity, as the current, generated by a DC source, appearing in parallel to a linear capacitor as well as to the volatile locally-active memristor, is subject to a monotonic increase.**

Keywords—Neuron, Hodgkin-Huxley Model, Hopf Supercritical Bifurcation, Hopf Subcritical Bifurcation, Saddle-Node Limit Cycle Bifurcation, Neuristor, Neuromorphic Engineering, Artificial Neural Networks, Artificial Intelligence, Local Activity, Edge of Chaos, Excitability, Threshold Switch, Memristor Technology

I. Introduction

Introduced by Mead [1] in 1989, the *neuromorphic engineering* field aims to design compact analogue electrical circuits and systems, which, operating according to similar principles as biological neuronal networks, may approach the energy efficiency of the human brain, while calculating solutions for some of the challenging problems it naturally solves. Major research results have been achieved since then on the development of bio-plausible circuit implementations of neurons and synapses [2] as well as on artificial neural networks with cognitive capabilities [3]-[4]. The recent availability of two classes of memristor physical realizations, one including non-volatile devices, which may be operated as finely-tuneable electronic synapses [5]-[6], and the other grouping two-terminal components, unable to store data under power-off conditions, but exhibiting a non-monotonic DC current versus voltage characteristic [7]-[8], similarly as the potassium [9] and sodium [10] ion channels across neuronal membranes, has opened up new opportunities in bio-inspired and neuromorphic circuit design. Focusing especially on the applications of the second class of memristive devices, which typically feature S-shaped DC loci, they have been employed to build electronic neurons [11]-[12], to reproduce complex nonlinear phenomena, including symmetry-breaking effects, accompanied by spatio-temporal pattern formation, in reaction-diffusion cellular networks through analogue electrical circuits, requiring fewer resources than their biological counterparts [13]-[14], to build cellular automata showcasing universal spike-based computing capability [15], and to design oscillatory arrays leveraging phase synchronization mechanisms to solve computationally-hard optimization problems [16]-[17].

Moreover, as reported in this manuscript, the capability of one of these volatile memristors [18], produced at NaMLab [19], to act as a source of infinitesimal energy, when poised anywhere along a branch of the respective DC current versus voltage characteristic, admitting a negative slope [20], a unique property also referred to as *Local Activity* [21], may be leveraged to develop the simplest ever-reported three-element analogue electrical cell [22] capable to experience, one after the other, the triplet of fundamental bifurcations, respectively governing the birth of a train of voltage spikes, their evolution, and their extinction via the All-to-None effect, emerging across neuronal axon membranes under a monotonic change in the net synaptic current, according to the predictions of the fourth-order bio-plausible Hodgkin-Huxley neuron model, while employing half the number of degrees of freedom as compared to the mathematical description of reference [23]. Drawing inspiration from a similar theoretical study, leading to the design of silicon neurons [24], this paper employs a dynamical system theory-based methodology [25] to tune the design parameters of the three-element cell in such a way to let it reproduce the bifurcation diagram of the Hodgkin-Huxley neuron model.

II. The concepts of local activity and edge of chaos

Let us consider a n^{th}-order one-port, endowed with a state vector of the form $\boldsymbol{x} \triangleq (x_1, \ldots, x_n) \in \mathbb{R}^n$, and a scalar input (scalar output) variable u (y), be defined via the differential algebraic equation (DAE) set

$$\dot{\boldsymbol{x}} = \boldsymbol{h}(\boldsymbol{x}, u, y), \text{ and} \quad (1)$$

$$H(\boldsymbol{x}, u, y) = 0, \quad (2)$$

where $\boldsymbol{h}(\cdot,\cdot): \mathbb{R}^n \times \mathbb{R} \to \mathbb{R}^n$ ($H(\cdot,\cdot,\cdot): \mathbb{R}^n \times \mathbb{R} \times \mathbb{R} \to \mathbb{R}$) expresses the state vector evolution function (an algebraic constraint between input, output, and state vector).

Let the input signal u be composed of the sum between two components, specifically a DC level U and an infinitesimal

signal δu, which adds up to the constant stimulus, applied to the two-terminal electrical element first, from some later time instant t_0. The state vector and the output voltage (current) variable of the one-port in response to the excitation signal u, assumed to be in current (voltage) form, will also consist of the sum between a constant component and a small-signal contribution, being respectively denoted as $\boldsymbol{x} = \boldsymbol{X} + \delta\boldsymbol{x}$ and $y = Y + \delta y$. The one-port is said to be *locally active* [21] about one operating point $\boldsymbol{Q} \triangleq (Q_1 \equiv X_1, \dots, Q_n \equiv X_n)$, at which it is preliminarily polarized through a certain DC stimulus $U = \widetilde{U}$, if and only if there exists a particular infinitesimal signal $\delta u(t) = \delta u^*(t)$, denoting a continuous function of time for all $t \geq t_0$, which triggers a state (output) solution to the one-port local model, featuring the initial condition $\delta\boldsymbol{x}(t_0) = \boldsymbol{0}$, in the form $\delta\boldsymbol{x}(t) = \delta\boldsymbol{x}^*(t)$ ($\delta y(t) = \delta y^*(t)$), such that, correspondingly, the infinitesimal energy $\delta\mathcal{E}(t_0, t; \boldsymbol{Q})$, absorbed by the one-port over a time frame (t_0, t), i.e.

$$\delta\mathcal{E}(t_0, t; \boldsymbol{Q}) = \int_{t_0}^{t} \delta u^*(t') \cdot \delta y^*(t') dt', \tag{3}$$

may assume a negative polarity at some time instant $t = \bar{t} > t_0$. Despite its rigor, this definition is not useful for testing purposes. Fortunately, however, the *Local Activity Theorem* [21] serves this purpose. Transforming the one-port local model in the Laplace domain, some algebraic manipulation allows to derive a closed-form expression for its local transfer function $F(s; \boldsymbol{Q}) \triangleq (\mathcal{L}\{\delta y(t)\}/\mathcal{L}\{\delta u(t)\})|_{\boldsymbol{Q}}$ about the respective operating point $\boldsymbol{Q}$ ($\mathcal{L}\{\cdot\}$ denotes the Laplace transform operator). If u denotes the one-port voltage v (current v), implying y to stand complementarily for the one-port current i (voltage v), $F(s; \boldsymbol{Q})$ corresponds to the one-port local admittance $Y(s; \boldsymbol{Q})$ (one-port local impedance $Z(s; \boldsymbol{Q})$) about $\boldsymbol{Q}$. The *Local Activity Theorem* establishes that a n^{th}-order one-port is locally-active about an operating point $\boldsymbol{Q}$ if and only if at least one of the four conditions to follow applies:

1) One pole of $F(s; \boldsymbol{Q})$, say the i^{th} one, denoted as $s = p_{i,F}(\boldsymbol{Q})$, where i may assume any integer value in the range $\{1,2,..n\}$, lies on the open Right Half Plane (RHP).

2) One pole of $F(s; \boldsymbol{Q})$, say the i^{th} one, denoted as $s = p_{i,F}(\boldsymbol{Q})$, where i may assume any integer value in the range $\{1,2,..n\}$, lies along the imaginary axis, i.e. $\Re\{p_{i,F}(\boldsymbol{Q})\} = 0$, while, concurrently, the respective residue, computed via $k_{p_{i,F}}(\boldsymbol{Q}) \triangleq \lim_{s \to p_{i,F}(\boldsymbol{Q})} (s - p_{i,F}(\boldsymbol{Q})) \cdot F(s; \boldsymbol{Q})$, is either a negative real-valued number or a complex number.

3) $F(s; \boldsymbol{Q})$ admits l poles, say $s = p_{k,F}(\boldsymbol{Q})$, $s = p_{k+1,F}(\boldsymbol{Q})$, …, $p_{k+l-1,F}(\boldsymbol{Q})$, which lie along the $j\omega$ axis, where l denotes an integer from the set $\{2, \dots, n\}$, and defines the range , where k may fall into, as $\{1, \dots, n - l + 1\}$.

4) The real part of $F(s; \boldsymbol{Q})$, evaluated for $s = j\omega$, assumes a negative value at some finite angular frequency $\omega = \omega_{0,F}(\boldsymbol{Q})$.

The *Edge of Chaos Corollary* [21] asserts that a n^{th}-order one-port is *on the Edge of Chaos* about one operating point $\boldsymbol{Q}$ if and only if two conditions simultaneously apply:

1) All the n poles of $F(s; \boldsymbol{Q})$ lie on the open Left Half Plane (LHP), i.e. $\Re\{p_{i,F}(\boldsymbol{Q})\} < 0$ for any integer value, assigned to the index i, from the set $\{1,2,..n\}$.

2) $\Re\{F(\omega; \boldsymbol{Q})\}$ becomes negative at some finite angular frequency $\omega = \omega_{0,F}(\boldsymbol{Q})$.

Therefore, in order to be on the Edge of Chaos about a given operating point $\boldsymbol{Q}$, the n^{th}-order one-port must necessarily be both *locally active and asymptotically stable* about it. Note that, while operating on the Edge of Chaos about some operating point, the one-port hides an *excitable condition* behind the quiescent state, which explains why it takes very small changes to any of its parameters or to its stimulus to trigger the destabilization of the quiet condition and the emergence of complex phenomena across its physical medium. According to the Hodgkin-Huxley model predictions, this is exactly what occurs to a neuron, when, sitting on a locally active and stable quiet state, experiences a Hopf Supercritical Bifurcation, destabilizing its operating point and spawning the development of stable infinitesimal sine-wave-alike oscillations across its membrane capacitance, under a tiny change in the net synaptic current.

III. The Hodgkin-Huxley Neuron

The fourth-order ordinary differential equation (ODE) [23], which Hodgkin and Huxley developed in the middle of the past century to model the giant neuronal axon membrane, characterizing a North Atlantic Sea squid, called *Loligo Pealeii*, admits the circuit-theoretic representation provided in Fig. 1, and reads as

$$\frac{dv_m}{dt} = \frac{1}{C} \cdot (i - i_K(n, v_K) - i_{Na}(m, h, v_{Na}) - i_L(v_L), \tag{4}$$

$$\frac{dn}{dt} = (1 - n) \cdot \alpha_n(v_m) - n \cdot \beta_n(v_m), \tag{5}$$

$$\frac{dm}{dt} = (1 - m) \cdot \alpha_m(v_m) - m \cdot \beta_m(v_m), \text{ and} \tag{6}$$

$$\frac{dh}{dt} = (1 - h) \cdot \alpha_h(v_m) - h \cdot \beta_h(v_m), \tag{7}$$

where v_m is the voltage, falling across the membrane capacitance C, n the activation gating variable of the first-order potassium (K) memristive ion channel, indicated as $\mathcal{M}_K$, m and h the activation and inactivation gating variables of the second-order sodium (Na) memristive ion channel $\mathcal{M}_{Na}$, respectively, and i the net synaptic current. The voltage-dependent functions, appearing in equations (5)-(7) are defined as

$$\alpha_n(v_m) = a_{\alpha_n} \cdot \frac{b_{\alpha_n} - v_m}{\exp\left(\frac{b_{\alpha_n} - v_m}{c_{\alpha_n}}\right) - 1}, \tag{8}$$

$$\beta_n(v_m) = a_{\beta_n} \cdot \exp\left(\frac{b_{\beta_n} - v_m}{c_{\beta_n}}\right), \tag{9}$$

$$\alpha_m(v_m) = a_{\alpha_m} \cdot \frac{b_{\alpha_m} - v_m}{\exp\left(\frac{b_{\alpha_m} - v_m}{c_{\alpha_m}}\right) - 1}, \tag{10}$$

$$\beta_m(v_m) = a_{\beta_m} \cdot \exp\left(\frac{b_{\beta_m} - v_m}{c_{\beta_m}}\right), \tag{11}$$

$$\alpha_h(v_m) = a_{\alpha_h} \cdot \exp\left(\frac{b_{\alpha_h} - v_m}{c_{\alpha_h}}\right), \text{ and} \tag{12}$$

$$\beta_h(v_m) = a_{\beta_h} \cdot \frac{1}{\exp\left(\frac{b_{\beta_h} - v_m}{c_{\beta_h}}\right) + 1}. \tag{13}$$

The currents through the K memristive ion channel, the Na memristive ion channel, and the resistive branch, accounting for leakage effects, are respectively expressed by

$$i_K(n, v_K) = \bar{g}_K \cdot n^4 \cdot v_K, \tag{14}$$

$$i_{Na}(m, h, v_{Na}) = \bar{g}_{Na} \cdot m^3 \cdot h \cdot v_{Na}, \text{ and} \tag{15}$$

$$i_L(v_L) = \bar{g}_L \cdot v_L, \tag{16}$$

where

$$v_K = v_m - E_K, \tag{17}$$

$$v_{Na} = v_m - E_{Na}, \text{ while} \tag{18}$$

$$v_L = v_m - E_L. \tag{19}$$

Importantly, E_K, E_{Na}, and E_L capture the effects of electrochemical gradients, which together contribute to set the DC bias points for the memristive ion channels.

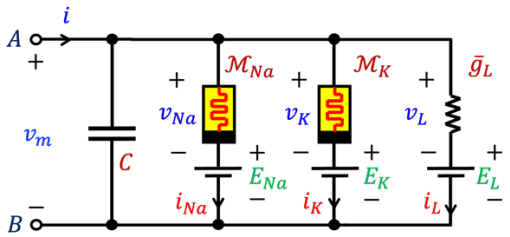

Fig. 1 Analogue electrical cell serving as circuit-theoretic representation for the fourth-order Hodgkin-Huxley neuron model.

TABLE I Model parameters of the Hodgkin-Huxley model (4)-(19).

$a_{\alpha_n}/(\text{mV}\cdot\text{ms})^{-1}$	b_{α_n}/mV	c_{α_n}/mV	$a_{\beta_n}/\text{ms}^{-1}$
0.01	10	10	0.125
b_{β_n}/mV	c_{β_n}/mV	$a_{\alpha_m}/(\text{mV}\cdot\text{ms})^{-1}$	b_{α_m}/mV
0	80	0.1	25
c_{α_m}/mV	$a_{\beta_m}/\text{ms}^{-1}$	b_{β_m}/mV	c_{β_m}/mV
10	4	0	18
$a_{\alpha_h}/\text{ms}^{-1}$	b_{α_h}/mV	c_{α_h}/mV	$a_{\beta_h}/\text{ms}^{-1}$
0.07	0	20	1
b_{β_h}/mV	c_{β_h}/mV	$\bar{g}_K/\text{mS}$	E_K/mV
30	10	36	−12
$\bar{g}_{Na}/\text{mS}$	E_{Na}/mV	$\bar{g}_L/\text{mS}$	E_L/mV
120	115	0.3	10.6

Using the parameter setting, reported in Table I [23], numerical simulations of equations (4)-(19) allow to determine all the possible stable and unstable quiescent and oscillatory steady states for the membrane capacitance voltage, after transients fade away, for each DC value I assigned to the net synaptic current i across the range $(0\text{A}, 180\mu\text{A})$. This numerical exploration produces the graph of Fig. 2, which appears in all classical textbooks on neuroscience, illustrating the most important *bifurcation diagram of the Hodgkin-Huxley neuron model*.

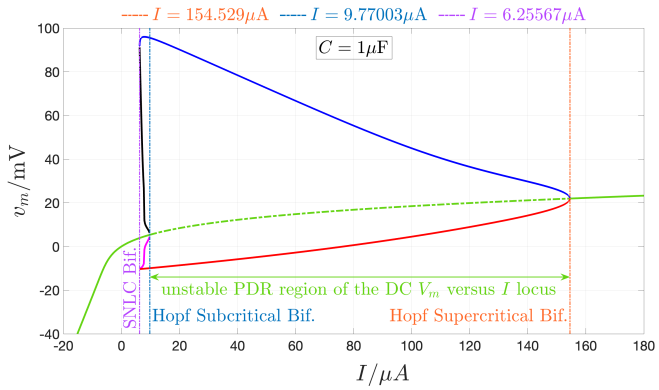

Fig. 2 Green trace: DC voltage V_m versus current I characteristic of the one-port appearing between the terminals A and B in Fig. 1. The entire locus features a positive slope, which endows the one-port with a strictly positive differential resistance (PDR). The solid (dash-dotted) branch includes stable (unstable) bias points for the one-port. Blue (Red) branch: maxima (minima) of stable steady-state oscillations in the membrane capacitance voltage v_m over the range of DC net synaptic currents, across which the one-port bias point $\boldsymbol{P}_{\mathcal{N}} = (V_m, I)$, i.e., equivalently, the neuron operating point $\boldsymbol{Q}_{\mathcal{N}} = (V_m, N, M, H)$, is unstable. Black (Magenta) branch: maxima (minima) of unstable oscillations, developing at steady state across the membrane capacitance in the narrow window of bias input currents, across which the neuron shows an interesting form of bi-stability, converging toward a quiescent state or exhibiting a spiking behavior after transients fade away. The capacitance C was set to 1μF. Under a monotonic decrease in the bias current stimulus I from 180μA to 0A, the neuron first experiences a *local Hopf Supercritical Bifurcation* [26], which destabilizes its operating point, while spawning infinitesimally-small sine-wave-alike stable oscillations across its capacitance, for $I = 154.529\mu\text{A}$. It is then subject to a *local Hopf Subcritical Bifurcation* [10], which restores the stability of its operating point, and concurrently gives birth to infinitesimally-small sine-wave-alike unstable oscillations across its capacitance, for $I = 9.77003\mu\text{A}$. Finally, it undergoes a *global Saddle-Node Limit Cycle* (SNLC) Bifurcation [27], at which the two cycles, which had been coexisting in the four-dimensional state space since the occurrence of the Hopf Subcritical Bifurcation, gently coalesce one into the other, for $I = 6.25567\mu\text{A}$. Bif. stands for Bifurcation.

After deriving a closed-form expression for the local input impedance $Z_{\mathcal{N}}(s; \boldsymbol{Q}_{\mathcal{N}})$ of the one-port, featuring terminals A and B, in the fourth-order circuit of Fig. 1, about one of its operating points, say $\boldsymbol{Q}_{\mathcal{N}} = (V_m, N, M, H)$, and recurring to the Local Activity Theorem and to the Edge of Chaos Corollary from section II, it can be demonstrated that the Hodgkin-Huxley neuron operates on the Edge of Chaos about the relevant operating point $\boldsymbol{Q}_{\mathcal{N}}$ when the net synaptic current I lies across the tiny windows $(154.529\mu\text{A}, 155.731\mu\text{A})$ and $(7.8293\mu\text{A}, 9.77003\mu\text{A})$. The lower (upper) bound in the first (second) of these current ranges corresponds to the local Hopf Supercritical (Subcritical) Bifurcation point in the diagram of Fig. 2.

IV. A LOCALLY-ACTIVE THRESHOLD SWITCH

A. Mathematical model

The ODE, governing the scalar state variable x, i.e. the internal temperature, of a first-order threshold switch produced at NaMLab is given by [18]

$$\dot{x} = g(x, v_m) \triangleq a_0 + a_1 \cdot x + (b_2 + c_{21} \cdot x + c_{22} \cdot x^2 + c_{23} \cdot x^3 + c_{24} \cdot x^4 + c_{25} \cdot x^5) \cdot v_m^2, \quad (20)$$

where $g(x, v_m)$ is the state evolution function, and v_m stands for the voltage, falling between the top and bottom Pt electrodes, which sandwich a double layer of the form NbO_x/Nb_2O_5 in the device physical stack [28]. The Ohm's law, expressing the dependence of the current i_m flowing through the device as a function of its voltage and state, reads as

$$i_m = i_m(x, v_m) \triangleq G_m(x) \cdot v_m = (d_0 + d_1 \cdot x + d_2 \cdot x^2 + d_3 \cdot x^3 + d_4 \cdot x^4) \cdot v_m, \quad (21)$$

where $G_m(x)$, whose formula is the state-dependent polynomial multiplying v_m on the rightmost side, denotes the memductance function.

Table II Parameter set for the fit [18] of the DAE set (20)-(21) to a switch with a stack structure of the form Pt/ Nb_2O_x/Nb_2O_5/Pt [28].

a_0	a_1	b_2	c_{21}
$5.19 \cdot 10^9$	$-2.05 \cdot 10^7$	$7.21 \cdot 10^9$	$-0.07 \cdot 10^9$
c_{22}	c_{23}	c_{24}	c_{25}
$+2.27 \cdot 10^5$	$-2.4 \cdot 10^2$	$1.25 \cdot 10^{-1}$	$-2.69 \cdot 10^{-5}$
d_0	d_1	d_2	d_3
$6.50 \cdot 10^{-3}$	$-6.66 \cdot 10^{-5}$	$2.14 \cdot 10^{-7}$	$-2.14 \cdot 10^{-10}$
d_4			
$1.19 \cdot 10^{-13}$			

Table II reports the values of the coefficients a_0, a_1, b_2, c_{21}, c_{22}, c_{23}, c_{24}, and c_{25} (d_0, d_1, d_2, d_3, and d_4) in the polynomial composing the state evolution function $g(x, v_m)$ (the device current function $i_m(x, v_m)$) in equation (20) ((21)).

B. Switch DC Response and Small-Signal or Local Model

Despite the model falls in the class of voltage-driven generic memristors, from a circuit-theoretic viewpoint the switch is a current-controlled device. In fact, letting any constant current

$i_m = I_m$ flow through its physical stack, one and only one bias voltage $v_m = V_m$ would be recorded between its terminals at steady state, as may be evinced by inspecting the device DC characteristic in Fig. 3. The device state x would concurrently converge toward a unique operating point $Q \triangleq X$, at which the state evolution function on the right-hand side of equation (20), with $v_m = R_m(x) \cdot I_m$ and $R_m(x) = G_m^{-1}(x)$, would vanish (see Fig. 4).

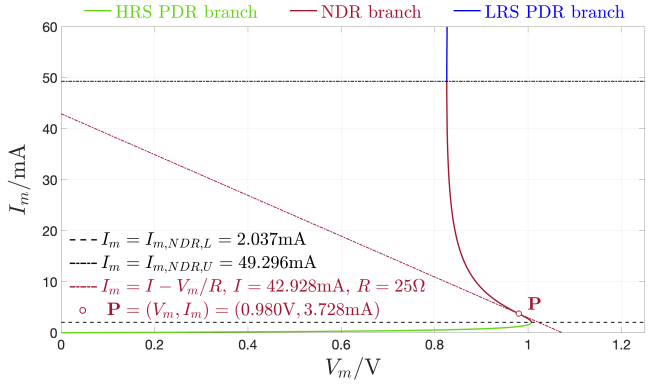

Fig. 3 S-shaped DC I_m versus V_m locus of the volatile memristor from NaMLab. The locus has a green, a brown, and a blue color along the High Resistance State (HRS) Positive Differential Resistance (PDR) branch, along the Negative Differential Resistance (NDR) branch, and along the Low Resistance State (LRS) PDR branch, respectively. The lower and upper bounds of the DC current range, across which the threshold switch admits a NDR, respectively are $I_{m,NDR,L} = 2.037mA$ and $I_{m,NDR,U} = 49.296mA$. Choosing a resistor with resistance $R = 25\Omega$ and a DC current stimulus $I = 42.928mA$ in the first-order cell from Fig. 6, the device is polarized on the bias point $\boldsymbol{P} = (V_m, I_m) = (0.980V, 3.728mA)$, where, correspondingly, its operating point Q is found to be equal to $411.386K$. The device bias point, marked through an open circle, lies at the intersection between the NDR branch of the S-shaped I_m versus V_m characteristic and the *DC load line* for the circuit of Fig. 6 (see the dashed brown trace), revealing the linear dependence of the current $I_m = I - V_m/R$, flowing through the device, upon the voltage V_m, falling between its terminals, under steady-state conditions, for $I = 42.928mA$ and $R = 25\Omega$.

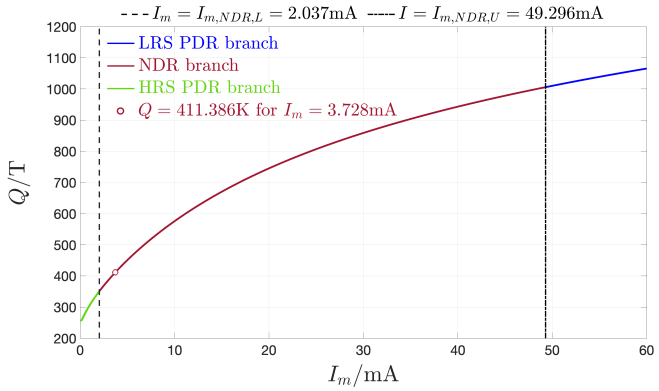

Fig. 4 Memristor operating point Q versus DC current I_m locus. For $I_m = 3.728$mA Q is found to be equal to 411.386K (see the circle marker).

Table III. Dependence of the coefficients in equations (22)-(23) upon Q.

$a(Q) \triangleq (\partial g/\partial x)\vert_{Q=X}$
$a_1 + V_m^2 \cdot (c_{21} + 2 \cdot c_{22} \cdot X + 3 \cdot c_{23} \cdot X^2 + 4 \cdot c_{24} \cdot X^3 + 5 \cdot c_{25} \cdot X^4)$
$b(Q) \triangleq (\partial g/\partial v_m)\vert_{Q=X}$
$2 \cdot (b_2 + c_{21} \cdot X + c_{22} \cdot X^2 + c_{23} \cdot X^3 + c_{24} \cdot X^4 + c_{25} \cdot X^5) \cdot V_m$
$c(Q) \triangleq (\partial i_m/\partial x)\vert_{Q=X}$
$(d_1 + 2 \cdot d_2 \cdot X + 3 \cdot d_3 \cdot X^2 + 4 \cdot d_4 \cdot X^3) \cdot V_m$
$d(Q) \triangleq (\partial i_m/\partial v_m)\vert_{Q=X}$
$G_m(X) = d_0 + d_1 \cdot x + d_2 \cdot x^2 + d_3 \cdot x^3 + d_4 \cdot x^4$

Developing $g(x, v_m)$ and $i_m(x, v_m)$ in Taylor series about an operating point $Q = X$ for the device, and then discarding the terms of order equal to or larger than two, allows to derive the device *small-signal or local model* [18]. The local parameters, appearing in the linearized variant of the DAE set (20)-(21), reading as

$$\delta\dot{x} = a(Q) \cdot \delta x + b(Q) \cdot \delta v_m, \text{ and} \quad (22)$$

$$\delta i_m = c(Q) \cdot \delta x + d(Q) \cdot \delta v_m, \quad (23)$$

depend upon the device operating point Q as reported in Table III. Transforming the DAE set (22)-(23) in the Laplace domain, some algebraic manipulation allows to derive the device small-signal impedance $Z_m(s; Q)$ about Q. In fact, we find

$$Z_m(s; Q) = \frac{\mathcal{L}\{\delta v_m(t)\}}{\mathcal{L}\{\delta i_m(t)\}}\Big|_Q = K_{Z_m}(Q) \cdot \frac{s - z_{Z_m}(Q)}{s - p_{Z_m}(Q)}, \quad (24)$$

in which the scaling factor K_{Z_m}, the zero z_{Z_m}, and the pole p_{Z_m} admit the expressions inferable from Table IV.

Table IV. Expressions for the three coefficients, appearing in equation (24), in terms of the operating point of the device via the electrical elements in its small-signal circuit model from Fig. 5.

$K_{Z_m}(Q) = r_1(Q)$
$z_{Z_m}(Q) = -r_2(Q)/l(Q)$
$p_{Z_m}(Q) = -(r_1(Q) + r_2(Q))/l(Q)$
$r_1(Q) = 1/d(Q)$
$r_2(Q) = -a(Q)/(b(Q) \cdot c(Q))$
$l(Q) = 1/(b(Q) \cdot c(Q))$

Fig. 5 shows a linear circuit, whose impedance at the port A − B, coincides with $Z_m(s; Q)$, provided the electrical elements, it hosts, depend upon the local parameters in (22)-(23) as tabulated in the last three rows of Table IV. Importantly, $r_1(Q)$ and $l(Q)$ are positive, irrespective of Q, whereas $r_2(Q)$ assumes a negative sign across the NDR branch of the device DC I_m versus V_m characteristic, featuring a positive polarity elsewhere. Moreover since $r_1(Q) + r_2(Q)$ is strictly positive, the Local Activity Theorem establishes that the NaMLab memristor operates on the Edge of Chaos at any bias point $\boldsymbol{P} = (V_m, I_m)$, lying along the NDR branch of the S-shaped I_m versus V_m locus, whereas it is locally passive anywhere on a PDR branch.

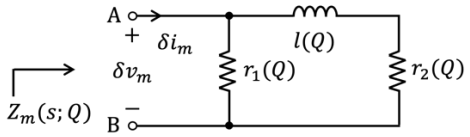

Fig. 5 Small-signal circuit model of the threshold switch about one of its operating points.

C. On the Switch Small-Signal Amplification Capability

Despite globally and locally passive electrical systems, such as the ideal transformer or the one-resistor-one-inductor-one-capacitor-one-voltage-source series circuit, may amplify signals, the local activity of the threshold switch from NaMLab allows to boost a small-signal stimulus in a circuit of unprecedented simplicity, which would be dumb otherwise [20]. When poised along the NDR branch of its DC current-voltage characteristic of Fig. 3, the Pt/Nb_2O_x/Nb_2O_5/Pt volatile threshold switch $\mathcal{M}$ shows the capability to act as a *source of infinitesimal energy*. For example, stabilizing the NaMLab device on the NDR bias point $\boldsymbol{P} = (V_m, I_m) =$

$(0.980\text{V}, 3.728\text{mA})$, indicated through a circle marker in Fig. 3, i.e., equivalently, on the operating point $Q = 411.386\text{K}$ (see the circle marker in Fig. 4), by connecting a resistor of resistance $R = 25\Omega$ and a current source i of DC level $I = 42.928\text{mA}$ between its terminals, as depicted in the circuit of Fig. 6, the local voltage δv_m (violet trace in Fig. 7), appearing across the switch in response to the second additive component in the stimulus i, specifically a purely-AC periodic sine-wave current δi (black trace in Fig. 7) of infinitesimal amplitude $\hat{\imath}$, set to $1\mu\text{A}$, and frequency f, fixed to $f_* = 1\text{MHz}$, admits a phase difference, relative to the memristor local current δi_m (blue trace in Fig. 7), of 118.042°, as can be computed at steady state via $\angle\delta v_m - \angle\delta i_m = -\omega_* \cdot \Delta T_*$, with ΔT_* standing for the difference, found to be equal to 672.106ns, between the time instant of a peak of level $\hat{v}_m = 27.617\mu\text{V}$ in δv_m and the time instant of the closest preceding peak of level $\hat{\imath}_m = 0.739\mu\text{A}$ in δi_m, while $\omega_* = 2 \cdot \pi \cdot f_*$, or, equivalently, via $\angle\delta v_m - \angle\delta i_m = \angle Z_m(j\omega_*; Q)$, where the threshold switch local impedance $Z_m(s; Q)$, evaluated at Q for $s = j\omega_*$, admits the modulus and phase response shown in blue and red in Fig. 8, respectively. As a result, omitting its DC behavior from the analysis, the threshold switch is found to generate some infinitesimal energy, indicated as $\delta\mathcal{E}(t, t + T_*; Q)$, about its operating point $Q = 411.386\text{K}$, over each local input cycle $(t, t + T_*)$, where $T_* = 1/f_* = 1\mu\text{s}$, at steady state, as may be inferred by inspecting the shape of the instantaneous local power $p_m = v_m \cdot i_m$ it absorbs after transients have decayed to zero (see the blue trace, residing on the lower half plane for most of the time across each period, in Fig. 9).

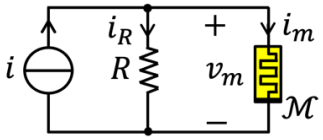

Fig. 6 A first-order analogue electrical cell, harnessing the capability of the threshold switch to generate local energy, when poised somewhere along the NDR branch of the respective DC I_m-V_m characteristic, for amplifying a small-signal sine-wave current superimposed on top of the bias stimulus.

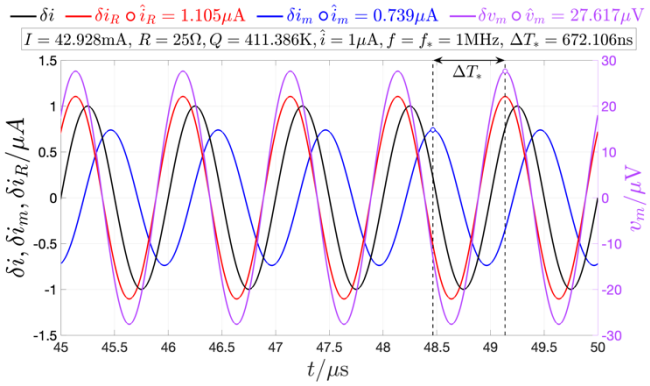

Fig. 7 Steady-state time course of the threshold switch local current δi_m (blue trace), of the resistor local current δi_R (red trace) and of the threshold switch local voltage δv_m (violet trace) in response to a purely-AC sine-wave current stimulus of the form $\delta i = \hat{\imath} \cdot \sin(2 \cdot \pi \cdot f \cdot t)$, with infinitesimal amplitude $\hat{\imath} = 1\mu\text{A}$ and frequency $f = f_* = 1\text{MHz}$ (black trace), in the analogue electrical cell of Fig. 6, where the DC stimulus $I = 42.928\text{mA}$ allows a constant current I_m of 3.728mA to flow continuously through the memristor $\mathcal{M}$. This simulation was obtained on the basis of the small-signal circuit model of the cell of Fig. 6, with the memristor described via the electrical system of Fig. 5 for $Q = 411.386\text{K}$, the DC source turned off, and the time instant t_0 of application of the local input current set to 0. A separate large-signal simulation of the cell from Fig. 6 confirmed the validity of the predictions drawn from the respective small-signal circuit model.

While the inclusion of the linear resistor is unnecessary for poising the locally-active threshold switch $\mathcal{M}$ at the earlier specified bias point $\boldsymbol{P}$, as simply connecting just a source of DC current 3.728mA across it would also serve the purpose, its introduction allows to build a simple small-signal current amplifier. As revealed in Fig. 10, denoting the Fourier transform operator as $\mathcal{F}\{\cdot\}$, the modulus of the *resistor-referred local transfer function*, defined as

$$H_R(j\omega; Q) \triangleq \frac{\mathcal{F}\{\delta i_R(t)\}}{\mathcal{F}\{\delta i(t)\}}\Big|_Q = \frac{Z_m(j\omega,Q)}{R+Z_m(j\omega,Q)}, \tag{25}$$

evaluated at the memristor operating point $Q = 411.386\text{K}$, is found to be larger than unity across the frequency range $(0, f_{|H_R|=1}(Q))$, where $f_{|H_R|=1}(Q) = 1529.956\text{kHz}$.

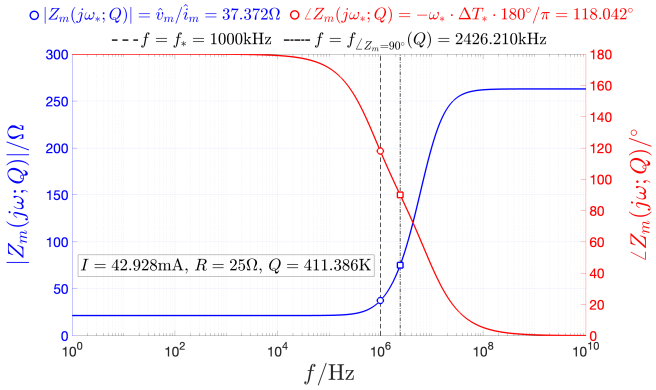

Fig. 8 Modulus (blue trace) and phase (red trace) of the local impedance $Z_m(j\omega; Q)$ of the NaMLab memristor about the operating point $Q = 411.386\text{K}$ as a function of the frequency f. The blue and red circle (square) markers respectively indicate the values for $|Z_m(j\omega; Q)|$ and $\angle Z_m(j\omega; Q)$ when f is equal to the input frequency f_* (to the frequency, referred to as $f_{\angle Z_m=90^\circ}(Q)$, at which the real part $\Re\{Z_m(j\omega; Q)\}$ of the device local impedance at Q, negative for smaller frequencies, increases up to 0).

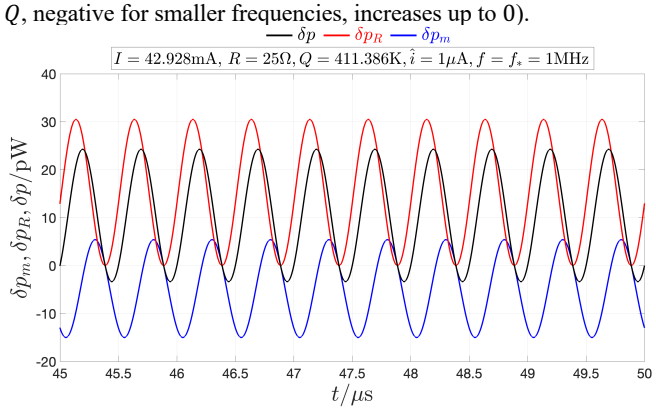

Fig. 9 Instantaneous local power generated by the small-signal current stimulus δi (black trace), and instantaneous local powers δp_m (blue trace) and δp_R (red trace) absorbed by the threshold switch $\mathcal{M}$ and by the resistor R, respectively, after transients fade away in the simulation, Fig. 7 refers to.

Additionally, local current gain may also be extracted through the memristive branch. In fact, the modulus of the *memristor-referred local transfer function*, defined as

$$H_m(j\omega; Q) \triangleq \frac{\mathcal{F}\{\delta i_m(t)\}}{\mathcal{F}\{\delta i(t)\}}\Big|_Q = \frac{R}{R+Z_m(j\omega,Q)}, \tag{26}$$

evaluated at the memristor operating point $Q = 411.386\text{K}$, exceeds positive one over the frequency range $(0, f_{|H_m|=1}(Q))$, where $f_{|H_m|=1}(Q) = 733.227\text{kHz}$.
Interestingly, both $f_{|H_m|=1}(Q)$ and $f_{|H_R|=1}(Q)$ are found to be smaller than the frequency $f_{\angle Z_m=90°}(Q) = \omega_{\angle Z_m=90°}/(2\cdot\pi)$, at which the phase $\angle Z_m(j\omega;Q)$ of the memristor local impedance $Z_m(j\omega;Q)$, larger than 90° for smaller frequencies, descends down to this critical angle (see the square marker on the red trace in Fig. 8).

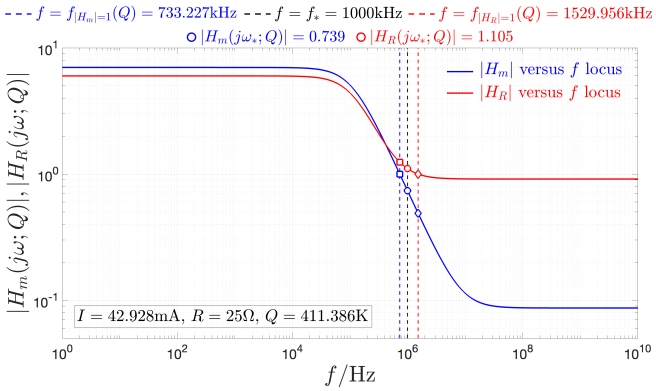

Fig. 10 Moduli of the resistor-referred local transfer function $H_R(j\omega;Q)$ (red trace, see equation (25)) and of the memristor-referred local transfer function $H_m(j\omega;Q)$ (blue trace, see equation (26)) against the frequency f. The blue and red square (diamond) markers respectively show the values for $|H_m(j\omega;Q)|$ and $|H_R(j\omega;Q)|$ when $f = \omega/(2\cdot\pi)$ equals $f_{|H_m|=1}(Q)$ ($f_{|H_R|=1}(Q)$). The blue red and circles in turn mark the levels of the resistor-referred and memristor-referred local transfer functions for $f = f_*$.

With reference to Fig. 7, once again, since, for $Q = 411.386\text{K}$, the input frequency f, set to $f_* = 1\text{MHz}$, falls inside the range $(f_{|H_m|=1}(Q), f_{|H_R|=1}(Q))$, the NDR effects, emerging across the nanodevice about the bias point $\boldsymbol{P} = (0.980\text{V}, 3.728\text{mA})$, allow to observe larger oscillations in the local sine-wave-alike current δi_R through the resistor (red trace) than in the small-signal sinusoidal current stimulus δi (black trace). As recorded in Fig. 7, the resistor local current amplitude $\hat{\imath}_R$ is larger than the small-signal current stimulus amplitude $\hat{\imath}$ by a factor equal to 1.105. This is predictable also through the formula $\hat{\imath}_R = \hat{\imath}\cdot|H_R(j\omega_*,Q)| = |Z_m(j\omega_*,Q)|/|R + Z_m(j\omega_*,Q)|$, applicable under the small-signal approximation hypothesis, using the calculations reported in Fig. 10. All in all, with reference to the first-order analogue electrical cell from Fig. 6, while acting as a source of local energy about the operating point $Q = 411.386\text{K}$, the threshold switch enables the resistive branch to boost the amplitude of small-signal input current oscillations of frequency $f = f_* = 1\text{MHz}$. An in-depth theoretical analysis, shedding light into the mechanisms underlying the complex nuances, some of which rather counterintuitive, in the small-signal amplification capabilities of the cell of Fig. 6, will be reported shortly in a Journal publication.

V. The Hodgkin-Huxley Neuristor

A. Cell Topology

Replacing the linear resistor of resistance R with a short circuit in the small-signal current amplification cell of Fig. 6, while adding a linear capacitor of capacitance C, across the locally-active memristor $\mathcal{M}$, results in the second-order analogue electrical circuit of Fig. 11 [22], which, as demonstrated shortly, requires just two degrees of freedom to reproduce qualitatively the bifurcation diagram of the fourth-order Hodgkin-Huxley neuron (see Fig. 2), and explains the origin for the name, specifically *Hodgkin-Huxley neuristor*, it will be addressed with hereafter.

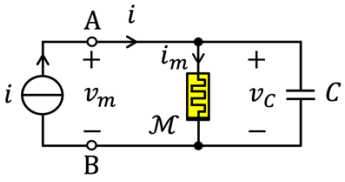

Fig. 11 Second-order analogue electrical cell, which, under a forward sweep in the DC current stimulus $i = I$, is capable to capture the cascade of the three fundamental neuronal bifurcations, occurring one after the other, under a monotonic decrease in the net synaptic current, inside a biological axon, according to the predictions of the fourth-order Hodgkin-Huxley neuron model, and signaling the most salient phases in the life cycle of a train of voltage spikes, also known as Action Potentials, across the neuronal membrane.

B. Large- and Small-Signal Cell Models and Their Analysis

The large-signal model of the Hodgkin-Huxley neuristor is the second-order ODE set

$$\dot{x} = g(x, v_m), \tag{27}$$

$$\dot{v}_m = \frac{i - i_m(x, v_m)}{C}, \tag{28}$$

where $g(x, v_m)$ and $i_m(x, v_m)$ are respectively defined in equations (20) and (21). For any given DC value I, assigned to the input current i, the right-hand sides of the two state equations (27) and (28) are found to vanish together when the memristor state x and voltage v_m assume the bias values $Q \equiv X$ and V_m, respectively, which defines a specific operating point, denoted as $\boldsymbol{Q}_{\mathcal{N}} = (Q, V_m)$, for the cell of Fig. 11. Replacing the memristor with its local circuit model from Fig. 5 into the cell of Fig. 11, and turning off the independent current source in the resulting circuit, the small-signal impedance of the one-port, featuring terminals A and B, evaluated at one of the operating points for the ODE set (27)-(28), say $\boldsymbol{Q}_{\mathcal{N}}$, is found to feature the formula

$$Z_{\mathcal{N}}(s;\boldsymbol{Q}_{\mathcal{N}}) = \frac{\mathcal{L}\{\delta v_m(t)\}}{\mathcal{L}\{\delta i(t)\}}\Big|_{\boldsymbol{Q}_{\mathcal{N}}} = \frac{K_{Z_{\mathcal{N}}}\cdot(s - z_{Z_{\mathcal{N}}}(\boldsymbol{Q}_{\mathcal{N}}))}{(s - p_{-,Z_{\mathcal{N}}}(\boldsymbol{Q}_{\mathcal{N}}))\cdot(s - p_{+,Z_{\mathcal{N}}}(\boldsymbol{Q}_{\mathcal{N}}))}, \tag{29}$$

where

$$K_{Z_{\mathcal{N}}} = 1/C, \tag{30}$$

$$z_{Z_{\mathcal{N}}}(\boldsymbol{Q}_{\mathcal{N}}) = -\frac{r_2(Q)}{l(Q)}, \text{ and} \tag{31}$$

$$p_{\mp,Z_{\mathcal{N}}}(\boldsymbol{Q}_{\mathcal{N}}) = \frac{\tau_{Z_{\mathcal{N}}}(\boldsymbol{Q}_{\mathcal{N}}) \mp \sqrt{\tau^2_{Z_{\mathcal{N}}}(\boldsymbol{Q}_{\mathcal{N}}) - 4\cdot\Delta_{Z_{\mathcal{N}}}(\boldsymbol{Q}_{\mathcal{N}})}}{2}, \tag{32}$$

with

$$\tau_{Z_{\mathcal{N}}}(\boldsymbol{Q}_{\mathcal{N}}) = -\frac{r_2(Q)}{l(Q)} - \frac{1}{C\cdot r_1(Q)}, \text{ and} \tag{33}$$

$$\Delta_{Z_{\mathcal{N}}}(\boldsymbol{Q}_{\mathcal{N}}) = \frac{r_1(Q) + r_2(Q)}{l(Q)\cdot C\cdot r_1(Q)}. \tag{34}$$

While $\Delta_{Z_{\mathcal{N}}}(\boldsymbol{Q}_{\mathcal{N}})$ keeps positive, irrespective of $\boldsymbol{Q}_{\mathcal{N}}$, $\tau_{Z_{\mathcal{N}}}(\boldsymbol{Q}_{\mathcal{N}})$ is positive if and only if $r_2(Q)$ is negative, and, concurrently, C is larger than a threshold value $\hat{C}(Q)$, depending on the memristor operating point Q, and defined as

$$\hat{C}(Q) \triangleq -\frac{l(Q)}{r_1(Q)\cdot r_2(Q)}. \tag{35}$$

It follows that the Hodgkin-Huxley neuristor operating point $\boldsymbol{Q}_{\mathcal{N}}$ is always stable if $r_2(Q) > 0$, while, when $r_2(Q) < 0$, it is stable only providing the inequality $C < \hat{C}(Q)$ holds true. The real part of the local impedance of the two-terminal

element at port A − B in the cell of Fig. 11, evaluated at $\boldsymbol{Q_N}$ and for $s = j\omega$, is expressed by

$$\Re\{Z_{\mathcal{N}}(j\omega;\boldsymbol{Q_N})\} = K_{Z_{\mathcal{N}}} \cdot \frac{(z_{Z_{\mathcal{N}}}(\boldsymbol{Q_N})-\tau_{Z_{\mathcal{N}}}(\boldsymbol{Q_N}))\cdot\omega^2 - z_{Z_{\mathcal{N}}}(\boldsymbol{Q_N})\cdot\Delta_{Z_{\mathcal{N}}}(\boldsymbol{Q_N})}{(\Delta_{Z_{\mathcal{N}}}(\boldsymbol{Q_N})-\omega^2)^2+(\omega\cdot\tau_{Z_{\mathcal{N}}}(\boldsymbol{Q_N}))^2}, \quad (36)$$

which goes negative if and only if the memristor is poised on the NDR branch of its DC characteristic, for

$$|\omega| = \left|\omega_{0,Z_{\mathcal{N}}}(\boldsymbol{Q_N})\right| < \omega_{0,Z_{\mathcal{N}},\max}(\boldsymbol{Q_N}) \triangleq \sqrt{\frac{-r_2(Q)\cdot(r_1(Q)+r_2(Q))}{l^2(Q)}}. \quad (37)$$

Applying the Local Activity Theorem and the Edge of Chaos Corollary from section II, the Hodgkin-Huxley neuristor is Stable and Locally-Active, i.e. on the Edge of Chaos, at the operating point $\boldsymbol{Q_N}$ if and only if $r_2(Q) < 0$, and $C < \hat{C}(Q)$. Combining all the results of the analysis, reported in this section, in an illustrative graphical form (refer to Fig. 12), the capacitance C versus DC input current I plane may be partitioned into regions of different colors, including parameter pairs, at which the cell of Fig. 11 is locally passive (grey area), locally active and stable, i.e. on the Edge of Chaos (ochre area), or locally active yet unstable (yellow area) about the respective operating point $\boldsymbol{Q_N}$, which is fixed through the DC stimulus (note that $I_m \equiv I$ and recall Fig. 4). Importantly, the black curve, dividing the regions of the C versus I parameter plane, where the cell is in turn locally active and unstable or locally active and stable about the respective operating point $\boldsymbol{Q_N}$, at which $r_2(Q)$ necessarily features a negative polarity, denotes the $\hat{C}(Q)$ versus I locus, along which a local Hopf Bifurcation occurs in the cell of Fig. 11. Importantly, for any capacitance larger than 872.824pF, denoting the ordinate of the minimum of this locus, the cell may undergo a local Hopf Bifurcation for either of two different DC values assigned to the respective input current. Moreover, the Supercritical or Subcritical nature of the Hopf Bifurcation, which the cell experiences along the black curve of Fig. 12, depends upon the particular choice for the design parameter pair (I, C).

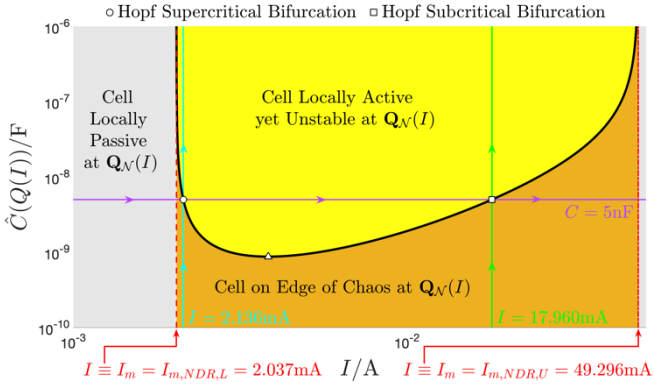

Fig. 12 Black trace: locus of the value of the capacitance $\hat{C}(Q(I))$, at which the cell of Fig. 11 undergoes a local Hopf Bifurcation, versus the respective DC current stimulus I. $\hat{C}(Q(I))$ exists if and only if the bias current through $\mathcal{M}$, coinciding with I, lies inside the NDR range $(I_{m,NDR,L}, I_{m,NDR,U}) = (2.037\text{mA}, 49.296\text{mA})$ (see Fig. 3). The triangle marker, indicating the minimum of the Hopf bifurcation curve, lies at $(I, C) = (3.842\text{mA}, 872.824\text{pF})$ ($Q(I)$ is here equal to 415K). The grey, ochre, and yellow regions include pairs for the circuit design parameters I and C, where the cell of Fig. 11 is respectively Locally Passive, Locally Active and Stable (i.e. on the Edge of Chaos), and Locally Active yet Unstable about the corresponding operating point $\boldsymbol{Q_N}$, which is fixed through the choice for the DC input current I reported on the horizontal axis. Interestingly, as will be clarified shortly, the three-element parallel cell of Fig. 11 may oscillate, for some values, assigned to the capacitance, even while operating on the Edge of Chaos under certain choices for I, as is the case when the DC current stimulus is set to 17.960mA. In these cases, the oscillations, developing across the second-order circuit, are induced by a global bifurcation phenomenon. Cyan (Green) vertical arrowed line: bifurcation path under a forward sweep in the capacitance for $I = 2.136$mA ($I = 17.960$mA). Violet horizontal arrowed line: bifurcation path under a forward sweep in the DC current stimulus for $C = 5$nF. The circle (square) marker indicates a pair of circuit design parameters, particularly $(I, C) = (2.136\text{mA}, 5\text{nF})$ $((17.960\text{mA}, 5\text{nF}))$, for which the cell of Fig. 11 experiences a local Hopf Bifurcation of Supercritical (Subcritical) form.

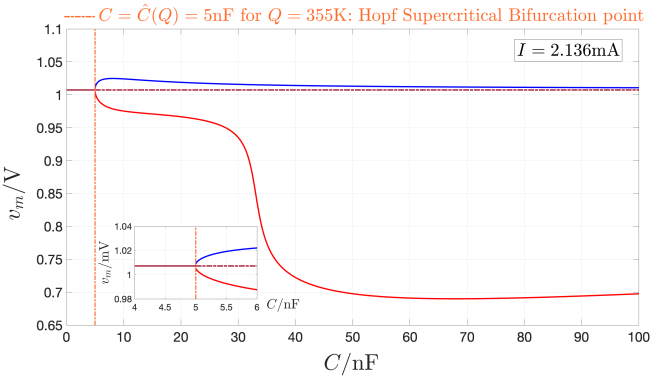

Fig. 13 Bifurcation diagram of the three-element cell of Fig. 11, described through the ODE set (27)-(28), under a forward sweep in the capacitance C from 0 to 100nF, for the scenario, where the DC current stimulus I is taken equal to 2.136mA (follow the corresponding vertical cyan-colored arrowed bifurcation path in the C versus I plane of Fig. 12). The cell undergoes a local Hopf Supercritical Bifurcation when C increases up to $5nF$ (see the inset). Any point on the brown solid (dashed) line $V_m = 1.007V$ indicates that the neuristor NDR operating point is stable (unstable) therein. See Fig. 2 for the significance of the blue and red traces.

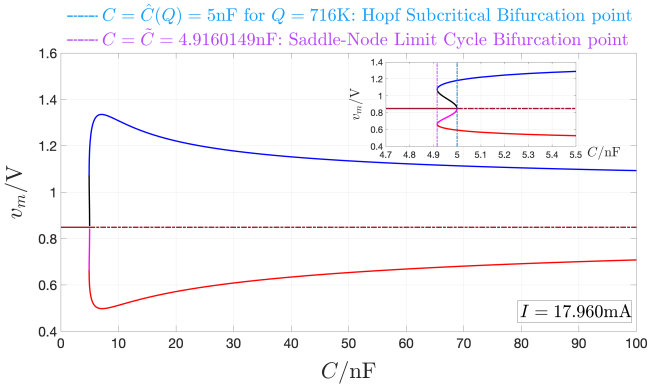

Fig. 14 Bifurcation diagram of the three-element cell of Fig. 11, described through the ODE set (27)-(28), under a forward sweep in the capacitance C from 0 to 100nF, for the scenario, where the DC current stimulus I is taken equal to 17.960mA (follow the corresponding vertical green-colored arrowed bifurcation path in the C versus I plane of Fig. 12). The cell undergoes a global Saddle-Node Limit Cycle Bifurcation when C attains the value of $\tilde{C} = 4.9160149nF$, while, shortly later, it experiences a local Hopf Subcritical Bifurcation when the circuit parameter under modulation becomes as large as $5nF$ (see the inset). Any point on the brown solid (dashed) line $V_m = 0.849V$ indicates that the neuristor NDR operating point is stable (unstable) therein. See Fig. 2 for the significance of the blue, red, black, and magenta traces.

Under a forward sweep in C, with I fixed to 2.136mA (17.960mA), which sets Q to 355K, i.e. following the vertical

cyan-colored (green-colored) arrowed bifurcation path in the capacitance versus DC input current plane from Fig. 12, the cell of Fig. 11 is found to experience a Hopf Supercritical (Subcritical) Bifurcation when the control parameter increases up to $\hat{C}(Q) = 5\text{nF}$, as illustrated in Fig. 13 (14). While the investigation of the small-signal model of the cell sheds light into its operating principles in the neighborhood of one of its operating points, the bifurcation analysis of the associated large-signal model also sheds light into its global behavior across the phase plane spanned by the state variables x and v_m. In fact, in the scenario Fig. 14 refers to, the bifurcation analysis revealed the occurrence of a global Saddle Node Bifurcation immediately before the emergence of the Hopf Subcritical Bifurcation, i.e., precisely, when C increased up to the value $\tilde{\text{C}} = 4.9160149\text{nF}$. Importantly, in this scenario there exists a tiny capacitance window, i.e. $(\tilde{C}, \hat{C}(Q))$, with $\hat{C}(Q) = 5\text{nF}$, where the cell is poised on the Edge of Chaos around some operating point $\boldsymbol{Q_{\mathcal{N}}}$, and yet, provided the initial condition to the ODE set (27)-(28) is positioned sufficiently away from the point attractor, it may lock in a non-silent spiking oscillatory mode at steady state. Having observed the emergence of the two local Hopf Bifurcations, occurring in the Hodgkin-Huxley neuron model, across the proposed second-order relaxation oscillator, under the injection of two different DC currents into the terminal A from Fig. 11, while keeping the capacitance unchanged, it was natural to explore its local and global nonlinear dynamics upon a monotonic modulation in the respective DC stimulus in the hypothesis to fix C exactly to 5nF, i.e. following the horizontal violet-colored arrowed bifurcation path in the C versus I plane of Fig. 12.

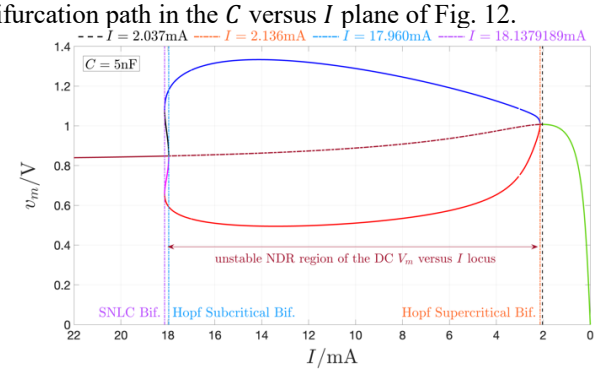

Fig. 15 Bifurcation diagram of the three-element second-order relaxation oscillator of Fig. 11, described through the ODE set (27)-(28), on the memristor voltage v_m versus DC input I current plane, in the scenario where the capacitance C is fixed to $5nF$. As its DC current stimulus is progressively increased from $0mA$ to $22mA$, the cell experiences first a local Hopf Bifurcation of Supercritical form when I attains the value of $2.136mA$, then a local Hopf Bifurcation of Subcritical form for $I = 17.960mA$, and, finally, shortly later, a global Saddle-Node Limit Cycle Bifurcation when the circuit parameter under forward sweep becomes as large as $18.1379189mA$. The green (brown) curve represents the PDR (NDR) branch of the DC V_m versus I locus of the one-port with terminals A and B in the cell of Fig 11. See Fig. 2 for the significance of the blue, red, black, and magenta traces.

The locus of quiescent and oscillatory steady states, recorded, as a result, for the memristor voltage v_m in the cell of Fig. 11 under a forward sweep in the respective bias input current I from 0mA to 22mA (see Fig. 15), qualitatively reproduces the bifurcation diagram of the Hodgkin-Huxley neuron model (refer to Fig. 2). Plots (a), (b)-(c), and (d) in Fig. 16 show the phase portraits of the second-order ODE system (27)-(28), modelling the three-element cell of Fig. 11, at the first, second, and third bifurcation points, indicated in Fig. 15, respectively. Importantly, as may be evinced by consulting the graphical illustration from Fig. 12, the three-element parallel circuit of Fig. 11 operates on frontier between Edge of Chaos (Unstable Local Activity) and Unstable Local Activity (Edge of Chaos) about the operating point $\boldsymbol{Q_{\mathcal{N}}} = (355\text{K}, 1.007\text{V})$ $(\boldsymbol{Q_{\mathcal{N}}} = (716\text{K}, 0.85\text{V}))$ at the local Hopf Supercritical (Subcritical) Bifurcation point $I = 2.136\text{mA}$ $(I = 17.960\text{mA})$.

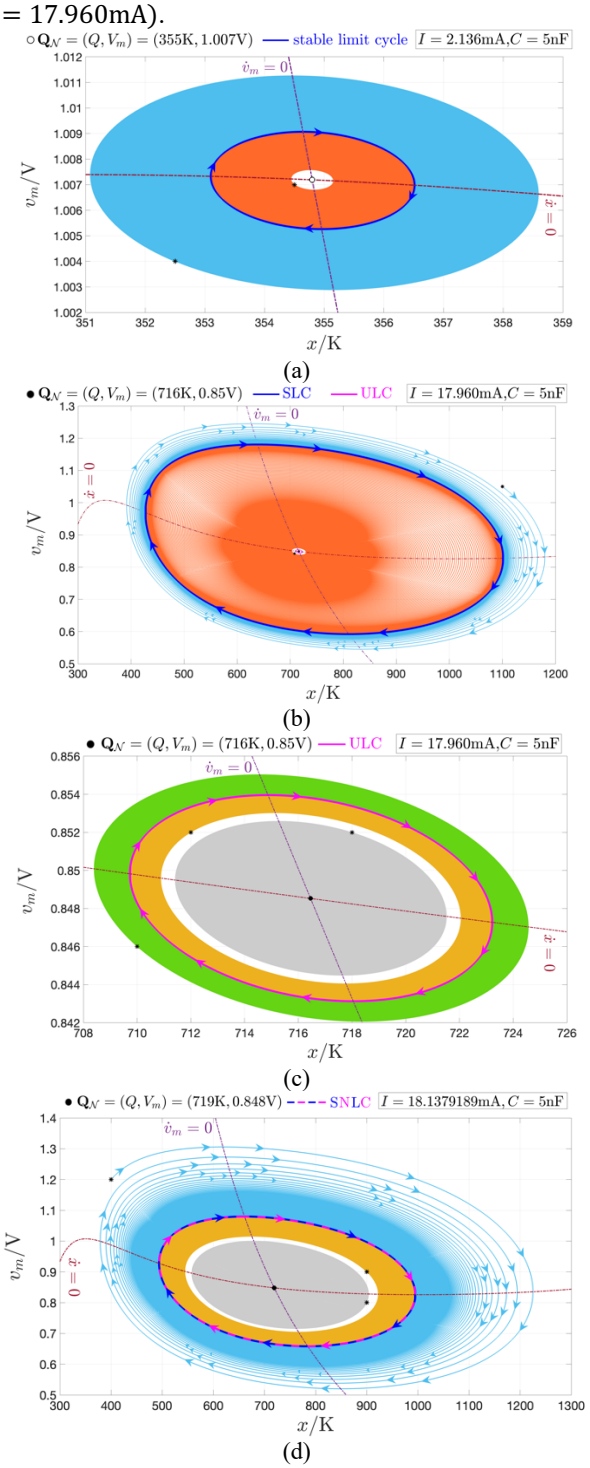

Fig. 16 Gallery of phase portraits of the ODE set (27)-(28), illustrating the local and global behavior of the memristive relaxation oscillator in Fig. 11 on the v_m versus x phase plane, for $C = 5\text{nF}$, at the local Hopf Supercritical Bifurcation, when $I =$

2.136mA (see plot (a)), at the local Hopf Subcritical Bifurcation, when $I = 17.960\text{mA}$ (see plots (b) and (c), the latter one being a close-up view of the first one in the region surrounding the unstable limit cycle), and at the global Saddle-Node Limit Cycle Bifurcation, when $I = 18.1379189\text{mA}$ (see plot (d)), respectively. A stable (An unstable) operating point $\boldsymbol{Q}_{\mathcal{N}} = (Q, V_m)$ for the cell is indicated through a black filled (hollow) circle marker. A blue (magenta) color is employed to indicate a stable (an unstable) limit cycle. At the SNLC bifurcation, responsible for the emergence of the All-to-None effect across the three-element cell of Fig. 11, a semi-stable isolated closed orbit, also referred to as Saddle-Node Limit Cycle, appears in the phase plane, as may be evinced from the phase portrait in plot (d), where it stands out for the alternating blue and magenta dashes it is traced with. Cyan- and orange-colored traces in (a) and (b) are forward-time phase-plane trajectories initiated within the basin of attraction of the SLC on its outside and inside, respectively. Grey-colored traces in plots (c) and (d) are forward-time phase-plane trajectories initiated within the basin of attraction of the operating point. The green-colored trace in plot (c) is a reverse-time phase-plane trajectory initiated within the basin of attraction of the SLC. The ochre-colored traces in plots (c) and (d) are reverse-time phase-plane trajectories initiated within the basin of attraction of the operating point. The cyan-colored trace in plot (d) is a forward-time phase-plane trajectory initiated outside the semi-stable limit cycle. Black asterisks in plots (a), (b), (c), and (d) mark the initial conditions for the numerical simulations producing the phase-plane trajectories departing from them. Acronyms' definitions follow: SLC stands for Stable Limit Cycle, ULC for Unstable Limit Cycle.

VI. Demonstration for the Robustness of the Dynamical System Theory-Based Circuit Design

In order to provide proof of evidence for the generality of the methodology, based on Dynamical System Theory [25], employed to design the Hodgkin-Huxley neuristor, this section demonstrates how the very same three-element parallel circuit of Fig. 11 is able to capture the cascade of three fundamental neuronal bifurcations, illustrated in Fig. 2, upon a monotonic modulation of the respective DC current stimulus, even under the hypothesis it hosts a different volatile locally active memristor from NaMLab. Here the memristor $\mathcal{M}$ from Fig. 11 is replaced by the circuit-theoretic model shown in Fig. 17. In regard to its mathematical formulation, capturing the nonlinear dynamics of a device, featuring a layer stack of the form Pt/Nb/NbOx/Pt [29] and smaller dimensions relative to the Pt/Nb_2O_x/Nb_2O_5/Pt sample [28], equations (20)-(21) were fitted to, the core switch, indicated as $\widetilde{\mathcal{M}}$, is modelled through a physics-based DAE set expressed by [17]

$$\frac{dT}{dt} = \tilde{g}(T, \tilde{v}_m) \triangleq \frac{\tilde{G}(T,\tilde{v}_m)}{C_{th}} \cdot \tilde{v}_m^2 - \frac{\Gamma_{th}}{C_{th}} \cdot (T - T_{\text{amb}}), \text{ and} \tag{38}$$

$$\tilde{\imath}_m = \tilde{G}(T, \tilde{v}_m) \cdot \tilde{v}_m, \text{ with} \tag{39}$$

$$\tilde{G}(T, \tilde{v}_m) \triangleq G_{01} \cdot \exp\left(-\frac{a_{01} - a_{11} \cdot |\tilde{v}_m|}{T}\right). \tag{40}$$

Two parasitic resistances are included in the model of the overall memristor device $\mathcal{M}$. First a nonlinear resistor $\mathcal{R}$, characterized by the implicit constitutive relationship

$$i_{\mathcal{R}} = G_{\mathcal{R}}(v_{\mathcal{R}}) \cdot v_{\mathcal{R}}, \text{ with} \tag{41}$$

$$G_{\mathcal{R}}(v_{\mathcal{R}}) \triangleq G_{02} \cdot \exp\left(-\frac{a_{02} - a_{12} \cdot \sqrt{|v_{\mathcal{R}}|}}{T_{\text{amb}}}\right), \tag{42}$$

appears in parallel to the core switch $\widetilde{\mathcal{M}}$. The resulting parallel one-port is then placed in series to a linear resistor R_C. Table V reports the parameter setting for the model of the overall memristor device $\mathcal{M}$, as resulting from the adaptation of the equation set (38)-(42) to a Pt/Nb/NbOx/Pt sample from NaMLab. As a result, the model for the Hodgkin-Huxley neuristor of Fig. 11 boils down to

$$\frac{dT}{dt} = \tilde{g}(T, \tilde{v}_m), \text{ and} \tag{43}$$

$$\dot{v}_m = \frac{i - i_m(T, \tilde{v}_m)}{C}, \tag{44}$$

where

$$i_m = (\tilde{G}(T, \tilde{v}_m) + G_{\mathcal{R}}(\tilde{v}_m)) \cdot \tilde{v}_m, \tag{45}$$

whereas v_m and $\tilde{v}_m$ must satisfy, at all times, the implicit algebraic constraint

$$v_C = \tilde{v}_m + \frac{\tilde{G}(T,\tilde{v}_m) + G_{\mathcal{R}}(\tilde{v}_m)}{G_C} \cdot \tilde{v}_m. \tag{46}$$

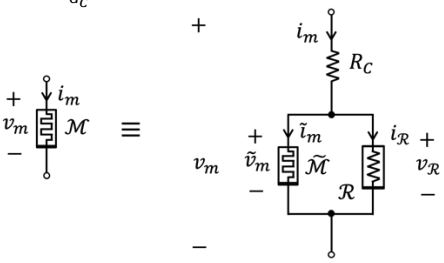

Fig. 17 Circuit-theoretic representation for the threshold switch $\mathcal{M}$ employed in the proposed electronic neuronal cell from Fig. 11 for the numerical investigations resulting in the bifurcation diagram of Fig. 18.

TABLE V. Parameter set for the fit [17] of the first-order extended memristor DAE set, composed of equations (38)-(42), to a device physical stack, where a double layer of the form Nb/NbOx [29] is sandwiched between two Pt electrodes.

C_{th}/F	$\Gamma_{th}/(\text{F}\cdot\text{s}^{-1})$	T_{amb}/K	G_{01}/S
$1 \cdot 10^{-14}$	$2.010 \cdot 10^{-6}$	293	0.395
a_{01}/K	$a_{11}/(\text{K}\cdot\text{V}^{-1})$	G_{02}/S	a_{02}/K
$3.841 \cdot 10^{3}$	$9.328 \cdot 10^{2}$	$1.285 \cdot 10^{-3}$	$1 \cdot 10^{3}$
$a_{12}/(\text{K}\cdot\text{V}^{-1/2})$		G_C/S	
$1.828 \cdot 10^{2}$		$5.269 \cdot 10^{-3}$	

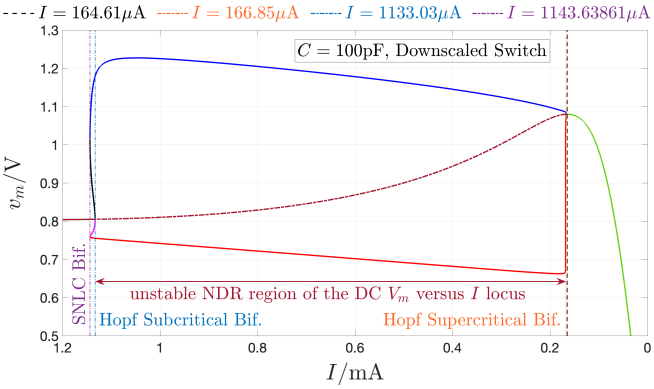

Fig. 18 Compact graphical representation illustrating all the possible stable and unstable quiescent and oscillatory steady states for the voltage v_m across the threshold switch $\mathcal{M}$ in the cell of Fig. 11, modelled via the large-signal DAE set model (43)-(46), as the respective bias input current I is progressively increased across the range $(0mA, 1.2mA)$, in the scenario where the capacitance C is chosen as small as $100pF$. During the forward sweep in the DC current stimulus, the cell is first subject to a local Hopf Supercritical Bifurcation, when I assumes the value of $166.85\mu A$, then a local Hopf Subcritical Bifurcation, for $I = 1133.03\mu A$, and shortly later, finally, a global Saddle-Node Limit Cycle Bifurcation, when the circuit parameter under one-way modulation reaches the critical level of $1143.63861\mu A$. Since the layer stack, the switch mathematical model (35)-(39) was fitted to, has smaller dimensions than the oxide film, the DAE set (20)-(21) was calibrated against, here the proposed three-element cell may act as a Hodgkin-Huxley neuristor under a lower DC energy budget than what was the case in the original circuit design (compare the v_m versus I locus, shown here, with the bifurcation diagram of Fig. 15).

Fig. 18 depicts all the possible quiescent and oscillatory steady states for the voltage v_m across the memristor device $\mathcal{M}$ in the cell of Fig. 11 for $C = 100\text{pF}$ as the DC current stimulus I is monotonically increased from 0mA to 1.2mA. Importantly, the reduced size of the memristor device, which the cell of Fig. 11 hosts here, allows to reduce the DC energy budget to be reserved for operating its three-element circuit as a Hodgkin-Huxley neuristor. In conclusion, the robustness of the proposed circuit design deserves to invest resources toward its experimental verification in the near future.

VII. Conclusions

This manuscript presents the first and simplest ever-reported three-element analogue electrical cell, which, leveraging the negative differential resistance of a single threshold switch, featuring a layer stack of the form Pt/ Nb_2O_x/Nb_2O_5/Pt, and produced at NaMLab, when energized through a suitable DC current source, requires only two degrees of freedom and a monotonic increase in the respective bias stimulus to undergo the very same cascade of three fundamental bifurcations, dictating the most salient phases in the life cycle of a train of voltage spikes, also known as Action Potentials, which a biological axon membrane experiences under a reverse sweep in the net synaptic current, according to the predictions of the bio-plausible fourth-order Hodgkin-Huxley neuron model. Powerful local analysis techniques from Nonlinear Dynamics Theory enable to explore the design parameter plane of the proposed cell, allowing the identification of a first (second) critical value for the DC current, subject to a progressive growth, at which, for a suitable capacitance choice, the proposed cell exits from the Stable yet Excitable Edge of Chaos regime (Unstable Local Activity domain) to enter the Unstable Local Activity domain (the Stable yet Excitable Edge of Chaos regime), triggering the occurrence of a Hopf Bifurcation of Supercritical (Subcritical) form, similarly as is the case for the Hodgkin-Huxley neuron model. Phase portrait investigations concurrently enabled the investigation of the global behavior of the cell during the forward sweep in the respective DC input current, which allowed the detection of the third critical neuronal phenomenon, referred to as Saddle-Node Limit Cycle Bifurcation, which induces the well-known All-to-None effect across its circuit. Upon a suitable recalibration of the capacitance, the very same three-element analogue electrical cell, proposed here, is able to reproduce the classical bifurcation diagram of the Hodgkin-Huxley neuron model also when the model of another locally-active device, fabricated at NaMLab with a layer stack of the form Pt/Nb/NbO_x/Pt, is employed to describe the switch.

References

[1] C.A. Mead, "Analog VLSI and Neural Systems," Addison Wesley, Reading (MA), 400pp., 1989, ISBN-13: 978-0201059922

[2] G. Indiveri, et al., "Neuromorphic silicon neuron circuits," Frontiers in neuroscience, vol. 5, no. 73, 23pp., 2011

[3] K. Boahen, "Neuromorphic Microchips," Scientific American, vol. 292, no. 5, pp. 56-63, 2005

[4] E. Chicca, et al., "Neuromorphic Electronic Circuits for Building Autonomous Cognitive Systems," Proceedings of the IEEE, vol. 102, no. 9, pp. 1367-1388, 2014

[5] G.W. Burr, et al., "Experimental Demonstration and Tolerancing of a Large-Scale Neural Network (165 000 Synapses) Using Phase-Change Memory as the Synaptic Weight Element," IEEE Trans. on Electron Devices, vol. 62, no. 11, pp. 3498-3507, 2015

[6] I. Boybat, et al., "Neuromorphic computing with multi-memristive synapses," Nature Communications, vol. 9, 2514(12pp.), 2018

[7] M.D. Pickett, and R.S. Williams, "Sub-100 fJ and sub-nanosecond thermally driven threshold switching in niobium oxide crosspoint nanodevices," Nanotechnology, vol. 23, no. 21, 215202(9pp.), 2012

[8] A. Ascoli, et al., "Nonlinear dynamics of a locally-active memristor," IEEE Trans. Circuits and Syst.-I (TCAS-I): Regular Papers, vol. 62, no. 4, pp. 1165-1174, 2015

[9] J.H. Wittig, Jr., and K. Boahen, "Potassium conductance dynamics confer robust spike-time precision in a neuromorphic model of the auditory brain stem," Journal of Neurophysiology, vol. 110, no. 2, pp. 307-321, 2013

[10] A. Ascoli, et al., "Edge of Chaos Theory Sheds Light into the All-or-None Phenomenon in Neurons - Part I: On the Fundamental Role of the Sodium Ion Channel," IEEE TCAS-I, vol. 71, no. 1, pp. 5-19, 2024

[11] M.D. Pickett, G. Medeiros-Ribeiro, and R.S. Williams, "A scalable neuristor built with Mott memristors," Nature Materials, vol. 12, no. 2, pp. 114-117, 2013, DOI: 10.1038/NMAT3510

[12] W. Yi, et al., "Biological plausibility and stochasticity in scalable VO2 active memristor neurons," Nature Communications, vol. 9, no. 4661, pp. 1-10, 2018

[13] A. Ascoli, et al., "Edge of Chaos is Sine Qua Non for Turing Instability," IEEE TCAS-I, vol. 69, no. 11, pp. 4596-4609, Nov. 2022

[14] A. Ascoli, et al., "Edge of Chaos Theory Resolves Smale Paradox," IEEE TCAS-I, vol. 69, no. 3, pp. 1252-1265, 2022

[15] M.D. Pickett, and R.S. Williams, "Phase transitions enable computational universality in neuristor-based cellular automata," Nanotechnology, vol. 24, 384002(7pp.), 2013

[16] S. Kumar, R.S. Williams, and Z. Wang, "Third-order nanocircuit elements for neuromorphic engineering," Nature, vol. 585, pp. 518-523, 2020

[17] M. Weiher, et al., "Improved Vertex Coloring With NbOx Memristor-Based Oscillatory Networks," IEEE TCAS-I, vol. 68, no. 5, pp. 2082-2095, 2021

[18] A. Ascoli, et al., "On Local Activity and Edge of Chaos in a NaMLab Memristor," Frontiers in Neuroscience, vol. 15, no. 651452, (30pp.), 2021

[19] https://www.namlab.com

[20] A. Ascoli, et al., "NDR Effects in a Locally-Active Memristor Induces Small-Signal Amplification in a Simple Cell," MOCAST, 2025

[21] L.O. Chua, "Local Activity is the Origin of Complexity," Int. J. on Bif. and Chaos (IJBC), vol. 15, no. 11, pp. 3435-3456, 2005

[22] A. Ascoli, et al., "Edge of Chaos Theory Unveils the First and Simplest Ever Reported Hodgkin-Huxley Neuristor," Adv. Ele. Mat., 2025, DOI:10.1002/aelm.202400789

[23] A.L. Hodgkin, and A.F. Huxley, "A quantitative description of membrane current and its application to conduction and excitation in nerve", J. Physiol., vol. 117, no. 4, pp. 500-544, 1952

[24] J.V. Arthur, and K.A. Boahen, "Silicon-Neuron Design: A Dynamical Systems Approach," IEEE TCAS-I, vol. 58, no. 5, pp. 1034-1043, 2011

[25] A. Ascoli, et al., "Analysis and Design of Bio-Inspired Circuits with Locally-Active Memristors," IEEE Trans. Circuits and Syst.-II (TCAS-II): Express Briefs, vol. 71, no. 3, pp. 1721-1726, 2024

[26] A.A. Andronov and C.E. Chaikin, "Theory of Oscillations," 347pp., Princeton University Press, Princeton, N.J., USA, 1949

[27] E.M. Izhikevich, "Neural excitability, spiking and bursting," IJBC, vol. 10, no. 6, pp. 1171-1266, 2000

[28] H. Mähne, et al., "Room temperature fabricated NbOx/Nb2O5 memory switching device with threshold switching effect," 5th IEEE International Memory Workshop, 2013

[29] M. Herzig, et al., "Multiple slopes in the negative differential resistance region of NbOx-based threshold switches," Journal of Physics D: Applied Physics, vol. 52, 325104(11pp.), 2019